

P-type Ohmic contact to monolayer WSe₂ field-effect transistors using high electron affinity amorphous MoO₃

Yi-Hsun Chen^{1,2,†}, Kaijian Xing^{1,†}, Song Liu³, Luke Holtzman⁴, Daniel L. Creedon⁵, Jeffrey C. McCallum⁵, Kenji Watanabe⁶, Takashi Taniguchi⁷, Katayun Barmak⁴, James Hone³, Alexander R. Hamilton⁸, Shao-Yu Chen^{2,9,}, Michael S. Fuhrer^{1,2,10*}*

¹ School of Physics and Astronomy, Monash University, Clayton, Victoria 3800, Australia

² Australian Research Council Centre of Excellence in Future Low-Energy Electronics Technologies (FLEET), Monash University, Clayton, Victoria 3800, Australia

³ Department of Mechanical Engineering, Columbia University, New York, New York 10027, United States

⁴ Department of Applied Physics and Applied Mathematics, Columbia University, New York, New York 10027, United States

⁵ School of Physics, the University of Melbourne, Melbourne, VIC 3010, Australia

⁶ Research Center for Functional Materials, National Institute for Materials Science, 1-1 Namiki, Tsukuba 305-0044, Japan

⁷ International Center for Materials Nanoarchitectonics, National Institute for Materials Science, 1-1 Namiki, Tsukuba 305-0044, Japan

⁸ School of Physics, University of New South Wales, 2052 Sydney, Australia

⁹ Center of Condensed Matter Sciences and Center of Atomic Initiative for New Material, National Taiwan University, Taipei 106, Taiwan

¹⁰ Monash Centre for Atomically Thin Materials, Monash University, Clayton, 3800, VIC, Australia

Keywords: Ohmic contact, contact resistance, monolayer WSe₂, molybdenum trioxide

(MoO₃), surface charge transferring, p-type semiconductor

ABSTRACT

Monolayer tungsten diselenide (1L-WSe₂) has been widely used for studying emergent physics due to the unique properties of its valence bands. However, electrical transport studies have been impeded by the lack of a reliable method to realize Ohmic hole-conducting contacts to 1L-WSe₂. Here, we report low-temperature p-type Ohmic contact between 1L-WSe₂ and molybdenum trioxide (MoO₃) where 1L-WSe₂ underneath MoO₃ is heavily hole doped through surface transfer doping. Electrical transport measurements reveal linear current-voltage relations at 10 K and nearly temperature-independent output curves up to room temperature, which support our finding. Furthermore, the contact resistivity of MoO₃-contacted 1L-WSe₂ FET is 25.9–66.2 kΩ·μm at a low carrier density of $1.5 \times 10^{12} \text{ cm}^{-2}$, which is the lowest reported for 1L-WSe₂ FETs. Realizing robust p-type Ohmic contact to a 2D transition metal dichalcogenide semiconductor will advance the development of microelectronics based on correlated phenomena in the valence bands.

Monolayer transition metal dichalcogenides (TMDs) have been extensively studied for their profound electronic and optoelectronic properties.^{1–5} Among the TMDs, monolayer WSe₂ (1L-WSe₂) is promising for investigating emergent physics arising in the valence band, owing to its low ionization potential^{6–8} and strong spin-orbit coupling resulting in fully spin-polarized valleys with large spin-splitting of 0.4 eV.^{9,10} 1L-WSe₂ has been used to study correlated physics^{11–15}, resonant tunneling¹⁶, and Bose-Einstein condensation^{17,18} in van der Waals heterostructures. However, studying these exotic phenomena through electronic transport often necessitates other techniques, such as capacitive^{19,20} or optical sensing^{12,15}, due to the difficulty in forming p-type Ohmic contacts to 1L-WSe₂. This issue becomes exponentially challenging at low temperatures.

A common strategy to fabricate Ohmic contact in conventional semiconductor devices is to dope the material underneath the contact heavily, for example, by ion implantation and subsequent high-temperature annealing²¹. However, such methods are not appropriate for atomically-thin van der Waal materials where the damage generated during implantation is hard to repair and can cause severe Fermi-level pinning²². Instead, surface transfer doping offers a favorable alternative, as it creates minimal defects in the material. Recently, surface transfer doping with transition metal oxides, such as MoO₃, WO₃, and V₂O₅, has been used to achieve high levels of p-doping in hydrogenated diamond^{23,24} and TMD^{25,26} based field-effect transistors (FETs).

In this work, we use amorphous MoO₃ as a surface transfer dopant to realize p-type Ohmic contacts to 1L-WSe₂ FETs. Electronic transport measurements on MoO₃-contacted 1L-WSe₂ FETs reveal Ohmic behavior, supported by linear and nearly temperature-independent output curves from room temperature to 10 K. We find that the contact resistance (R_c) is about 1.8–4.6 k Ω (contact resistivity 25.9–66.2 k $\Omega\cdot\mu\text{m}$) at a carrier density of $1.5 \times 10^{12} \text{ cm}^{-2}$, the lowest among those reported for 1L-WSe₂ FETs in hole transport regime. Examination of the

activation barriers for bulk and contacts shows that activated behavior is dominated by the bulk even for carrier densities into the subthreshold regime. The realization of p-type Ohmic contacts enables high-quality 1L-WSe₂ FETs and further paves the way to developing quantum electronic devices based on correlated quantum phenomena in WSe₂ valence bands.

Figures 1a and 1b show schematically the relative positions of the electronic bands of MoO₃ and 1L-WSe₂ and the resulting junction at the contact regime in equilibrium. The electron affinity of MoO₃ (6.7 eV)²⁷ is higher than the ionization potential of 1L-WSe₂ (4.8–5.2 eV)^{6–8}, resulting in p-doping of the WSe₂. Here we consider MoO₃ as a highly-doped n-type semiconductor, while some previous works have treated it as a metal with a high work function^{28,29}. The spontaneous charge transfer between MoO₃ and 1L-WSe₂ increases the electron (hole) density in MoO₃ (1L-WSe₂), leading to a non-rectifying barrier with no depletion region at the interface between the doped contact region and the pristine channel (Figure 1b). Moreover, MoO₃ has a lower deposition temperature of about 475°C, compared to traditional high work function metals (Pd, Pt, and Au), which may moderate the impacts of evaporated atoms on the 1L-WSe₂ and maintain a high-quality interface by minimizing disorder-induced gap states.^{30,31}

We first confirm surface transfer doping by performing low-temperature photoluminescence (LT-PL). Figures 1c and 1d show the LT-PL spectra of 1L-WSe₂ at 80 K before and after depositing MoO₃, respectively. In Figures 1c and 1d, the PL spectrum is composed of two distinct peaks: the high-energy one is from the neutral excitons, and the lower-energy one is from trions (a neutral exciton bound to a free charged carrier). For pristine 1L-WSe₂ (Figure 1c) the energy separation of these two peaks is about 34 meV, corresponding to the binding energy of negative trions (X⁻, exciton bound to a free electron).³² The presence of X⁻ indicates the n-type doping of as-prepared 1L-WSe₂. In contrast, after depositing MoO₃ (Figure 1d), the binding energy of trions changes to 18 meV, consistent with positive trions (X⁺, exciton bound

to a free hole).^{32,33}. The significant alteration of trion species from negative to positive trions demonstrates the significant p-type surface transfer doping of 1L-WSe₂ by MoO₃.

Figure 2a shows the optical micrograph of a MoO₃ contacted 1L-WSe₂ FET with hBN encapsulation. The detailed fabrication processes can be found in Supporting Information S1. Briefly, 1L-WSe₂/hBN heterostructures were firstly fabricated using WSe₂ crystals grown by the self-flux method³⁴. After that, we deposited 20 nm MoO₃ and 60 nm Pd in sequence through typical photolithography, then transferred a top hBN layer to improve the sample stability. We note that hBN encapsulation effectively reduces extrinsic Coulomb scatterers from both ambient and the SiO₂/Si substrate³⁵. In addition, depositing Pd can enhance electrical conduction and further protect MoO₃ from degradation; the work function of MoO₃ decreases when exposed to the ambient due to the reduction of oxygen vacancies³⁶. The cross-sectional schematic of MoO₃ contacted 1L-WSe₂ FETs is shown in Figure 2b. Control devices were fabricated similarly with electrodes of 60 nm Pd only.

Figure 3 shows the output characteristics of a MoO₃ contacted 1L-WSe₂ FET and the control device at various gate voltages (V_{gs}) and temperatures. The measurements are conducted by applying a source-drain voltage (V_{ds}) across two outer electrodes and simultaneously measuring the drain current (I_{ds}) and the four-probe voltage (V_{4p}). Figure 3a shows low-bias ($|V_{ds}| \leq 100$ mV) output curves of the MoO₃ contacted 1L-WSe₂ FET at $T = 10$ K for different V_{gs} . It exhibits a typical behavior of hole conduction, where the threshold voltage (V_{th}) is estimated as -68 V (see Figure S3a). The output curves are linear and symmetric for a wide range of V_{gs} , suggesting robust Ohmic behavior of MoO₃-contacted 1L-WSe₂ even at such low temperature. Notably, the linear current-voltage relationship can be observed even in the subthreshold region ($V_{gs} > -68$ V). The linear output curves indicate any energy barrier at the metal-semiconductor interface smaller than a few times the thermal energy $k_B T = 0.86$ meV, where k_B is the Boltzmann constant. As a comparison in Figure 3b, the control device exhibits nonlinear output

curves at $T = 10$ K with a much lower output current at the same V_{gs} , suggesting that a sizable energy barrier limits the conduction. Since the devices were fabricated identically except for the contacts, we attribute the outstanding output characteristics in the MoO_3 contacted 1L- WSe_2 FET to the Ohmic contact formed at the $\text{MoO}_3/1\text{L-WSe}_2$ interface.

Figures 3c and 3d show temperature-dependent output curves at $V_{gs} = -80$ V for both devices. The MoO_3 contacted 1L- WSe_2 FET exhibit linear output curves with little temperature dependence over a wide temperature range ($T = 10$ – 250 K), consistent with the observation of a negligible activation barrier. This is significant in contrast to the control device, whose output curves become more resistive and highly nonlinear below $T = 100$ K, indicating that considerable thermal energy is required to overcome the Schottky barrier. We note that the conductivity of the MoO_3 -contacted 1L- WSe_2 FET slightly decreases below $T = 150$ K. This might be due to the temperature dependence of V_{th} (Supporting Information S4): The V_{th} shifts negatively when temperature decreases, resulting in a reduction of induced free carrier density in WSe_2 .

We quantitatively model the current flow in our MoO_3 contacted 1L- WSe_2 FETs in order to extract R_c . Figure 4a shows the two-probe conductance $G_{2p} = I_{ds}/V_{ds}$ and four-probe conductance $G_{4p} = I_{ds}/V_{4p}$ as a function of V_{gs} at $T = 77$ K. Both curves present a typical turn-on behavior with $V_{th} = -58$ V (see Figure S3b). The G_{4p} is about 3 times higher than G_{2p} , consistent with the ratio of the channel length: $19 \mu\text{m}$ for V_{ds} probes and $7 \mu\text{m}$ for V_{4p} probes. Furthermore, we found that the two-probe (μ_{2p}) and four-probe mobilities (μ_{4p}) extracted from two- and four-terminal measurements are almost identical: μ_{2p} is $56.1 \text{ cm}^2/\text{V}\cdot\text{s}$ and μ_{4p} is $61.2 \text{ cm}^2/\text{V}\cdot\text{s}$ at $|V_{gs} - V_{th}| = 17$ V. Both results imply that the MoO_3 -contacted devices exhibit small R_c , consistent with the previous discussion in Figure 3. Note that we are only able to present G_{4p} at $V_{gs} \leq -33$ V because of instrumental limitation when the channel becomes highly resistive in our setup.

Typically, R_c can be extracted from four-terminal measurements by calculating

$$2R_c = R_{2p} - \alpha R_{4p} \quad (1),$$

where R_{2p} and R_{4p} are the two- and four-probe resistance, respectively; α is geometry factor. For an ideal Hall bar geometry, $\alpha = L_{2p}/L_{4p}$ can be treated as a constant and R_c can be calculated straightforwardly using Eqn. (1), where L_{4p} is the length between V_{4p} electrodes and L_{2p} is the length between V_{ds} electrodes. However, it is critical to consider the device geometry in the case when the V_{4p} probes are invasive. For instance, some current may flow through the electrodes, making the determination of α uncertain. Moreover, α may depend on contact resistance as it affects the relative distribution of current flowing through the sample and electrodes.

To tackle the above issues, we determine R_c by performing finite-element modelling by COMSOL simulation (see Supporting Information S6). We considered a two-dimensional model where electrodes (MoO_3/Pd in our case) are embedded in the channel. As illustrated in Figures S6a and S6b, the device geometry is determined by the nominal dimensions of the photolithography pattern. The TMD-metal contacts can be modelled by a width of d within the nominal electrode boundary. These marginal regions account for both “transfer length” under electrodes and any dimensional differences from nominal patterns caused by under/overexposure. In addition, we assigned the conductivity of channel material (σ_{channel}), contact regions (σ_c), and metal (σ_m) independently. σ_{channel} can be approximated from the two-terminal conductance $\sigma_{\text{channel}} = G_{4p} \times \frac{L_{2p}}{W}$, where W is the width of the channel, since the contact resistance is small in the MoO_3 contacted 1L-WSe₂ FET. σ_m is approximated by the conductivity of Pd: $\sigma_m = 4.8 \times 10^5$ S. With this model, R_c can be calculated as $R_c = \frac{1}{\sigma_c} \frac{W}{d}$ given σ_c and d . We cannot determine σ_c and d unambiguously from a single measurement of the ratio of V_{4p}/V_{ds} at each V_{gs} and T . However, d should be smaller than one-half the electrode width

and cannot be significantly negative (corresponding to actual electrodes wider than nominal dimensions) as this would be apparent in optical microscopy. Fortunately, we find in our calculations that d must be at least a small positive value (e.g. 183 nm at $V_{\text{gs}} = -80$ V and $T = 77$ K), and that the $\sigma_c/\sigma_{\text{channel}}$ for which $V_{4\text{p}}/V_{\text{ds}}$ matches the experiment does not depend strongly on d . Therefore, we are able to strongly bound the values of σ_c (and hence R_c) that are consistent with the measurement.

Figure 4b shows calculated R_c as a function of temperature at V_{gs} ranging from -60 to -80 V. R_c is strongly dependent on V_{gs} but only weakly dependent on temperature, as expected for a negligible activation barrier. At $T = 77$ K, we found R_c approximately 1.8–4.6 k Ω at $V_{\text{gs}} = -80$ V. According to the conventional parallel plate capacitance approximation, $n = C_{\text{ox}} |V_{\text{gs}} - V_{\text{th}}|/q$, the corresponding carrier density (n) at $V_{\text{gs}} = -80$ V is 1.5×10^{12} cm $^{-2}$ ($|V_{\text{gs}} - V_{\text{th}}| = 22$ V). It is worth noting that this is the first work to demonstrate p-type Ohmic contact to 1L-WSe $_2$ at a low carrier density ($n = 1.5 \times 10^{12}$ cm $^{-2}$). The $R_c = 1.8$ –4.6 k Ω (or contact resistivity 25.9–66.2 k $\Omega \cdot \mu\text{m}$) is favorable compared to previously reported 1L-WSe $_2$ FETs,³⁷ and comparable to Co/hBN tunneling contact in monolayer MoS $_2$ ³⁸. The R_c dependence on temperature is also sensitive to different V_{gs} . At a small negative V_{gs} , R_c is weakly sensitive to temperature. However, R_c is almost independent of temperature at a high V_{gs} , such as $V_{\text{gs}} = -80$ V. This can be attributed to a higher conductivity of 1L-WSe $_2$ underneath MoO $_3$ while applying a high V_{gs} .

In Figure 4c, we compare R_c by two methods mentioned above: COMSOL simulation and Eqn. (1). We set $\alpha = 2.7$ determined by the ratio of the physical distances between the V_{ds} and $V_{4\text{p}}$ electrodes to calculate R_c based on Eqn. (1). We found the result acquired by the naïve application of Eqn. (1) overestimates R_c about 2 times at $V_{\text{gs}} = -80$ V and underestimates R_c at $V_{\text{gs}} \geq -77$ V compared to the simulation. The failure of Eqn. (1) results from the assumption that the device has an ideal Hall bar geometry with a constant α , leading to an incorrect

estimation of R_c when it is applied to a device with invasive V_{4p} electrodes. Our results emphasize the significance of considering the geometry factor to estimate R_c in a device with non-ideal geometry.

We provide further evidence of an Ohmic contact between MoO_3 -doped WSe_2 and the WSe_2 channel by measuring the activation barriers for the contacts and the channel as a function of V_{gs} separately. We estimate the activation barrier of the contacts Φ_{2p} using the standard thermionic emission model³⁹:

$$\sigma_{ds} = A^* T^{3/2} \exp\left[-\frac{\Phi_{2p}}{k_B T}\right] \left[1 - \exp\left(\frac{qV_{ds}}{k_B T}\right)\right],$$

where A^* is Richardson's constant, q is the elementary charge, k_B is the Boltzmann constant, and T is the temperature. Φ_{2p} is the energy required to overcome the contact barrier *via* the thermionic emission process, which can be extracted by fitting the slope in the Arrhenius plot at each V_{gs} . We estimate the activation barrier of the WSe_2 channel by assuming that the four-probe conductivity σ_{4p} is thermally activated, i.e. $\sigma_{4p} \propto e^{-\Phi_{4p}/k_B T}$, where Φ_{4p} is the activation energy (energy difference between Fermi energy and valence band edge or mobility edge) in the WSe_2 channel.

Figures 5a and 5b show Arrhenius plots of σ_{4p} and $\sigma_{ds}/T^{3/2}$ for the MoO_3 contacted 1L- WSe_2 FET, respectively. The Φ_{4p} is 22 meV at $V_{gs} = -34$ V and then decreases to 3 meV at $V_{gs} = -80$ V, as shown in Figure S5a. The point at which Φ_{4p} becomes smaller than thermal energy $k_B T$ (8.6 meV for $T = 100$ K) marks a transition from thermally activated (sub-threshold) behavior at $V_{gs} \geq -50$ V to relatively temperature-independent conduction at $V_{gs} \leq -50$ V, which agrees reasonably well with the estimated V_{th} in Supporting Information S3. Figure 5c shows the activation barriers of bulk and contacts, Φ_{4p} and Φ_{2p} , as functions of V_{gs} extracted from Arrhenius plots of σ_{4p} and $\sigma_{ds}/T^{3/2}$, respectively (Figures 5a,b). The observations are surprising, and at odds with the conventional picture in the case of a Schottky barrier at the metal-

semiconductor interface³⁹, as illustrated in Figure 5d: At small negative V_{gs} (orange lines, Figure 5d), the bulk barrier dominates conduction, and $\Phi_{4p} \approx \Phi_{2p}$. As the V_{gs} is tuned more negative (blue and green lines, Figure 5d), the bulk barrier Φ_{4p} becomes smaller but the contact barrier Φ_{2p} saturates at the Schottky barrier height. Figure 5e shows that, in contrast, for the interface between a heavily p-doped semiconductor contact and a gate-controlled semiconductor channel, the condition $\Phi_{4p} = \Phi_{2p}$ is expected at the flat-band condition and $\Phi_{4p} \approx \Phi_{2p}$ is expected at V_{gs} beyond the flat-band condition.

Examining the V_{gs} dependence of Φ_{4p} and Φ_{2p} (Figure 5c), the observations are consistent with an Ohmic contact between a heavily p-doped semiconductor contact and the gate-controlled channel (Figure 5e). In particular, we find that Φ_{4p} is comparable to Φ_{2p} at $V_{gs} \leq -37$ V ($|\Phi_{2p} - \Phi_{4p}| \leq k_B T \approx 8.6\text{--}17.2$ meV at $T = 100\text{--}200$ K). Moreover, we never observe a regime in which Φ_{2p} saturates while Φ_{4p} decreases with increasingly negative V_{gs} , as typically observed for Schottky barrier contacts. At more negative V_{gs} , Φ_{2p} appears even to drop below Φ_{4p} , and is undetectable for $V_{gs} \leq -46$ V, even though bulk activation is still evident (the device is in the subthreshold regime). This possibly reflects the smooth nature of the contact barrier (Figure 5e) or difficulty in measuring thermionic emission for $\Phi_{2p} \leq k_B T$. The practical result is that the temperature dependence due to thermionic emission at the contacts is negligible for all V_{gs} above threshold, and even well into the subthreshold regime. We also measured a Pd-only contacted 1L-WSe₂ control device (Figure 5f), which shows clear thermal activation in a higher temperature range (200 K $\leq T \leq 300$ K) with Φ_{2p} remaining large at V_{gs} values at which the barrier in the MoO₃-contacted device is negligible.

In conclusion, we have demonstrated that surface transfer doping by MoO₃ can be used to create p-type Ohmic contacts to 1L-WSe₂ enabling low-temperature transport measurements. Furthermore, we have shown that finite element modeling is surprisingly useful for extracting the contact resistance in devices with a non-standard geometry such as invasive contacts,

simplifying the fabrication of devices for contact resistance measurements. Our surface transfer doping strategy is simple to implement and should be broadly applicable to other van der Waals layered semiconductors, as well as heterostructures and twisted-layer structures, enabling electronic transport studies of novel correlated phenomena in the valence bands of 2D semiconductors.

ASSOCIATED CONTENT

Supporting Information.

The Supporting Information is available free of charge.

S1. Device fabrication of 1L-WSe₂ field-effect transistors for electrical transport measurements and MoO₃/1L-WSe₂ heterostructure for photoluminescence spectroscopy

S2. Scanning tunneling spectroscopic measurement of WSe₂ crystals

S3. Estimation of threshold voltage for 1L-WSe₂ FETs

S4. Drain current as a function of $|V_{gs} - V_{th}|$

S5. Estimation of activation energy of 1L-WSe₂ FETs

S6. Calculation of contact resistance by using finite element method.

AUTHOR INFORMATION

Corresponding Author(s)

Michael S. Fuhrer – School of Physics and Astronomy and Australian Research Council Centre of Excellence in Future Low-Energy Electronics Technologies (FLEET), Monash University, Clayton, Victoria 3800, Australia; ORCID iD: <https://orcid.org/0000-0001-6183-2773>; Email: michael.fuhrer@monash.edu

Shao-Yu Chen – Center of Condensed Matter Sciences and Center of Atomic Initiative for New Material, National Taiwan University, Taipei 106, Taiwan; Australian Research Council Centre of Excellence in Future Low-Energy Electronics Technologies (FLEET), Monash University, Clayton, Victoria 3800, Australia; ORCID iD: <https://orcid.org/0000-0003-3423-9768>; Email: shaoyuchen@ntu.edu.tw

Authors

Yi-Hsun Chen – School of Physics and Astronomy and Australian Research Council Centre of Excellence in Future Low-Energy Electronics Technologies (FLEET), Monash University, Clayton, Victoria 3800, Australia; ORCID iD: <https://orcid.org/0000-0001-6313-5189>

Kaijian Xing – School of Physics and Astronomy, Monash University, Clayton, Victoria 3800, Australia; ORCID iD: <https://orcid.org/0000-0001-5254-4710>

Song Liu – Department of Mechanical Engineering, Columbia University, New York, New York 10027, United States

Luke Holtzman – Department of Applied Physics and Applied Mathematics, Columbia University, New York, New York 10027, United States

Daniel L. Creedon – School of Physics, the University of Melbourne, Melbourne, VIC 3010, Australia

Jeffrey C. McCallum – School of Physics, the University of Melbourne, Melbourne, VIC 3010, Australia

Kenji Watanabe – Research Center for Functional Materials, National Institute for Materials Science, 1-1 Namiki, Tsukuba 305-0044, Japan

Takashi Taniguchi – International Center for Materials Nanoarchitectonics, National Institute for Materials Science, 1-1 Namiki, Tsukuba 305-0044, Japan

Katayun Barmak – Department of Applied Physics and Applied Mathematics, Columbia University, New York, New York 10027, United States

James Hone – Department of Mechanical Engineering, Columbia University, New York, New York 10027, United States

Alexander R. Hamilton – School of Physics, University of New South Wales, 2052 Sydney, Australia

Author Contributions

†These authors contributed equally. Y. H. Chen, K. Xing, S. Y. Chen, and M. S. Fuhrer conceived and designed this project. Y. H. Chen fabricated the devices with assistance from K. Xing with the MoO₃ and Pd deposition. Y. H. Chen performed the device characterization, data analysis, and finite element modeling. K. Xing provided the concept of utilizing high electron affinity MoO₃ to surface transfer dope 1L-WSe₂. S. Y. Chen performed the low-temperature photoluminescence measurement. S. Liu, J. Hone, L. N. Holtzman, and K. Barmak provided the WSe₂ crystals. D. L. Creedon, J. C. McCallum provided the resources. The manuscript was written through contributions of all authors. All authors have given approval to the final version of the manuscript.

Notes

The authors declare no competing financial interest.

ACKNOWLEDGMENT

Y. H. Chen thanks Mr. Pei-Wei Chi for insightful discussion regarding the finite element method. Tungsten diselenide crystal growth was supported under the United States National Science Foundation Materials Research Science and Engineering Center through grants DMR-1420634 and DMR-2011738. Y. H. Chen, A. R. Hamilton, M. S. Fuhrer, and S. Y. Chen acknowledge support from the ARC Centre of Excellence in Future Low-Energy Electronics Technologies (FLEET; CE170100039). K. Watanabe and T. Taniguchi acknowledge support from the JSPS KAKENHI (Grant Numbers 19H05790, 20H00354 and 21H05233). S. Y. Chen acknowledges support from the Center of Atomic Initiative for New Materials, National Taiwan University (grant nos. 110 L9008 and 111 L9008), from the Featured Areas Research Center Program within the framework of the Higher Education Sprout Project by the Ministry of Education of Taiwan. K. Xing acknowledges support from ARC grant DP200101345. S. Y.

Chen thanks the experimental support from Dr. Li-Chyong Chen and Dr. Yu-Ling Liu in the Center of Condensed Matter Sciences at National Taiwan University, and Dr. Wei-Hua Wang in the Institute of Atomic and Molecular Sciences, Academia Sinica. This work was performed in part at the Melbourne Centre for Nanofabrication (MCN) in the Victorian Node of the Australian National Fabrication Facility (ANFF).

REFERENCES

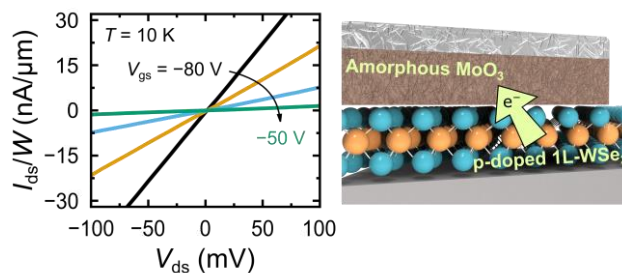
- (1) Manzeli, S.; Ovchinnikov, D.; Pasquier, D.; Yazyev, O. V.; Kis, A. 2D Transition Metal Dichalcogenides. *Nat. Rev. Mater.* **2017**, *2* (8), 1–15. <https://doi.org/10.1038/natrevmats.2017.33>.
- (2) Fogler, M. M.; Butov, L. V.; Novoselov, K. S. High-Temperature Superfluidity with Indirect Excitons in van Der Waals Heterostructures. *Nat. Commun.* **2014**, *5* (1), 4555. <https://doi.org/10.1038/ncomms5555>.
- (3) Ahn, E. C. 2D Materials for Spintronic Devices. *Npj 2D Mater. Appl.* **2020**, *4* (1), 1–14. <https://doi.org/10.1038/s41699-020-0152-0>.
- (4) Wang, Q. H.; Kalantar-Zadeh, K.; Kis, A.; Coleman, J. N.; Strano, M. S. Electronics and Optoelectronics of Two-Dimensional Transition Metal Dichalcogenides. *Nat. Nanotechnol.* **2012**, *7* (11), 699–712. <https://doi.org/10.1038/nnano.2012.193>.
- (5) Xiao, D.; Liu, G.-B.; Feng, W.; Xu, X.; Yao, W. Coupled Spin and Valley Physics in Monolayers of MoS₂ and Other Group-VI Dichalcogenides. *Phys. Rev. Lett.* **2012**, *108* (19), 196802. <https://doi.org/10.1103/PhysRevLett.108.196802>.
- (6) Gong, C.; Zhang, H.; Wang, W.; Colombo, L.; Wallace, R. M.; Cho, K. Band Alignment of Two-Dimensional Transition Metal Dichalcogenides: Application in Tunnel Field Effect Transistors. *Appl. Phys. Lett.* **2013**, *103* (5), 053513. <https://doi.org/10.1063/1.4817409>.
- (7) Kang, J.; Tongay, S.; Zhou, J.; Li, J.; Wu, J. Band Offsets and Heterostructures of Two-Dimensional Semiconductors. *Appl. Phys. Lett.* **2013**, *102* (1), 012111. <https://doi.org/10.1063/1.4774090>.
- (8) Rasmussen, F. A.; Thygesen, K. S. Computational 2D Materials Database: Electronic Structure of Transition-Metal Dichalcogenides and Oxides. *J. Phys. Chem. C* **2015**, *119* (23), 13169–13183. <https://doi.org/10.1021/acs.jpcc.5b02950>.
- (9) Riley, J. M.; Mazzola, F.; Dendzik, M.; Michiardi, M.; Takayama, T.; Bawden, L.; Granerød, C.; Leandersson, M.; Balasubramanian, T.; Hoesch, M.; Kim, T. K.; Takagi, H.; Meevasana, W.; Hofmann, P.; Bahramy, M. S.; Wells, J. W.; King, P. D. C. Direct Observation of Spin-Polarized Bulk Bands in an Inversion-Symmetric Semiconductor. *Nat. Phys.* **2014**, *10* (11), 835–839. <https://doi.org/10.1038/nphys3105>.
- (10) Mak, K. F.; Shan, J. Photonics and Optoelectronics of 2D Semiconductor Transition Metal Dichalcogenides. *Nat. Photonics* **2016**, *10* (4), 216–226. <https://doi.org/10.1038/nphoton.2015.282>.
- (11) Li, E.; Hu, J.-X.; Feng, X.; Zhou, Z.; An, L.; Law, K. T.; Wang, N.; Lin, N. Lattice Reconstruction Induced Multiple Ultra-Flat Bands in Twisted Bilayer WSe₂. *Nat. Commun.* **2021**, *12* (1), 5601. <https://doi.org/10.1038/s41467-021-25924-6>.
- (12) Jin, C.; Tao, Z.; Li, T.; Xu, Y.; Tang, Y.; Zhu, J.; Liu, S.; Watanabe, K.; Taniguchi, T.; Hone, J. C.; Fu, L.; Shan, J.; Mak, K. F. Stripe Phases in WSe₂/WS₂ Moiré Superlattices. *Nat. Mater.* **2021**, *20* (7), 940–944. <https://doi.org/10.1038/s41563-021-00959-8>.
- (13) Arora, H. S.; Polski, R.; Zhang, Y.; Thomson, A.; Choi, Y.; Kim, H.; Lin, Z.; Wilson, I. Z.; Xu, X.; Chu, J.-H.; Watanabe, K.; Taniguchi, T.; Alicea, J.; Nadj-Perge, S. Superconductivity in Metallic Twisted Bilayer Graphene Stabilized by WSe₂. *Nature* **2020**, *583* (7816), 379–384. <https://doi.org/10.1038/s41586-020-2473-8>.
- (14) Wang, L.; Shih, E.-M.; Ghiotto, A.; Xian, L.; Rhodes, D. A.; Tan, C.; Claassen, M.; Kennes, D. M.; Bai, Y.; Kim, B.; Watanabe, K.; Taniguchi, T.; Zhu, X.; Hone, J.; Rubio, A.; Pasupathy, A. N.; Dean, C. R. Correlated Electronic Phases in Twisted Bilayer Transition Metal Dichalcogenides. *Nat. Mater.* **2020**, *19* (8), 861–866. <https://doi.org/10.1038/s41563-020-0708-6>.

- (15) Scuri, G.; Andersen, T. I.; Zhou, Y.; Wild, D. S.; Sung, J.; Gelly, R. J.; Bérubé, D.; Heo, H.; Shao, L.; Joe, A. Y.; Mier Valdivia, A. M.; Taniguchi, T.; Watanabe, K.; Lončar, M.; Kim, P.; Lukin, M. D.; Park, H. Electrically Tunable Valley Dynamics in Twisted WSe₂/WSe₂ Bilayers. *Phys. Rev. Lett.* **2020**, *124* (21), 217403. <https://doi.org/10.1103/PhysRevLett.124.217403>.
- (16) Kim, K.; Prasad, N.; Movva, H. C. P.; Burg, G. W.; Wang, Y.; Larentis, S.; Taniguchi, T.; Watanabe, K.; Register, L. F.; Tutuc, E. Spin-Conserving Resonant Tunneling in Twist-Controlled WSe₂-HBN-WSe₂ Heterostructures. *Nano Lett.* **2018**, *18* (9), 5967–5973. <https://doi.org/10.1021/acs.nanolett.8b02770>.
- (17) Wang, Z.; Rhodes, D. A.; Watanabe, K.; Taniguchi, T.; Hone, J. C.; Shan, J.; Mak, K. F. Evidence of High-Temperature Exciton Condensation in Two-Dimensional Atomic Double Layers. *Nature* **2019**, *574* (7776), 76–80. <https://doi.org/10.1038/s41586-019-1591-7>.
- (18) Shan, H.; Lackner, L.; Han, B.; Sedov, E.; Rupprecht, C.; Knopf, H.; Eilenberger, F.; Beierlein, J.; Kunte, N.; Esmann, M.; Yumigeta, K.; Watanabe, K.; Taniguchi, T.; Klemmt, S.; Höfling, S.; Kavokin, A. V.; Tongay, S.; Schneider, C.; Antón-Solanas, C. Spatial Coherence of Room-Temperature Monolayer WSe₂ Exciton-Polaritons in a Trap. *Nat. Commun.* **2021**, *12* (1), 6406. <https://doi.org/10.1038/s41467-021-26715-9>.
- (19) Xu, Y.; Liu, S.; Rhodes, D. A.; Watanabe, K.; Taniguchi, T.; Hone, J.; Elser, V.; Mak, K. F.; Shan, J. Correlated Insulating States at Fractional Fillings of Moiré Superlattices. *Nature* **2020**, *587* (7833), 214–218. <https://doi.org/10.1038/s41586-020-2868-6>.
- (20) Ma, L.; Nguyen, P. X.; Wang, Z.; Zeng, Y.; Watanabe, K.; Taniguchi, T.; MacDonald, A. H.; Mak, K. F.; Shan, J. Strongly Correlated Excitonic Insulator in Atomic Double Layers. *Nature* **2021**, *598* (7882), 585–589. <https://doi.org/10.1038/s41586-021-03947-9>.
- (21) Rideout, V. L. A Review of the Theory and Technology for Ohmic Contacts to Group III–V Compound Semiconductors. *Solid-State Electron.* **1975**, *18* (6), 541–550. [https://doi.org/10.1016/0038-1101\(75\)90031-3](https://doi.org/10.1016/0038-1101(75)90031-3).
- (22) Liu, Y.; Guo, J.; Zhu, E.; Liao, L.; Lee, S.-J.; Ding, M.; Shakir, I.; Gambin, V.; Huang, Y.; Duan, X. Approaching the Schottky–Mott Limit in van Der Waals Metal–Semiconductor Junctions. *Nature* **2018**, *557* (7707), 696–700. <https://doi.org/10.1038/s41586-018-0129-8>.
- (23) Xing, K.; Xiang, Y.; Jiang, M.; Creedon, D. L.; Akhgar, G.; Yianni, S. A.; Xiao, H.; Ley, L.; Stacey, A.; McCallum, J. C.; Zhuiykov, S.; Pakes, C. I.; Qi, D.-C. MoO₃ Induces P-Type Surface Conductivity by Surface Transfer Doping in Diamond. *Appl. Surf. Sci.* **2020**, *509*, 144890. <https://doi.org/10.1016/j.apsusc.2019.144890>.
- (24) Xing, K.; Zhang, S.; Tsai, A.; Xiao, H.; Creedon, D. L.; Yianni, S. A.; McCallum, J. C.; Pakes, C. I.; Qi, D.-C. High-Electron-Affinity Oxide V₂O₅ Enhances Surface Transfer Doping on Hydrogen-Terminated Diamond. *Diam. Relat. Mater.* **2020**, *108*, 107865. <https://doi.org/10.1016/j.diamond.2020.107865>.
- (25) Yamamoto, M.; Nakaharai, S.; Ueno, K.; Tsukagoshi, K. Self-Limiting Oxides on WSe₂ as Controlled Surface Acceptors and Low-Resistance Hole Contacts. *Nano Lett.* **2016**, *16* (4), 2720–2727. <https://doi.org/10.1021/acs.nanolett.6b00390>.
- (26) Cai, L.; McClellan, C. J.; Koh, A. L.; Li, H.; Yalon, E.; Pop, E.; Zheng, X. Rapid Flame Synthesis of Atomically Thin MoO₃ down to Monolayer Thickness for Effective Hole Doping of WSe₂. *Nano Lett.* **2017**, *17* (6), 3854–3861. <https://doi.org/10.1021/acs.nanolett.7b01322>.

- (27) Meyer, J.; Hamwi, S.; Kröger, M.; Kowalsky, W.; Riedl, T.; Kahn, A. Transition Metal Oxides for Organic Electronics: Energetics, Device Physics and Applications. *Adv. Mater.* **2012**, *24* (40), 5408–5427. <https://doi.org/10.1002/adma.201201630>.
- (28) Chuang, S.; Battaglia, C.; Azcatl, A.; McDonnell, S.; Kang, J. S.; Yin, X.; Tosun, M.; Kapadia, R.; Fang, H.; Wallace, R. M.; Javey, A. MoS₂ P-Type Transistors and Diodes Enabled by High Work Function MoO_x Contacts. *Nano Lett.* **2014**, *14* (3), 1337–1342. <https://doi.org/10.1021/nl4043505>.
- (29) Zhou, C.; Zhao, Y.; Raju, S.; Wang, Y.; Lin, Z.; Chan, M.; Chai, Y. Carrier Type Control of WSe₂ Field-Effect Transistors by Thickness Modulation and MoO₃ Layer Doping. *Adv. Funct. Mater.* **2016**, *26* (23), 4223–4230. <https://doi.org/10.1002/adfm.201600292>.
- (30) Jang, J.; Ra, H.-S.; Ahn, J.; Kim, T. W.; Song, S. H.; Park, S.; Taniguchi, T.; Watanabe, K.; Lee, K.; Hwang, D. K. Fermi-Level Pinning-Free WSe₂ Transistors via 2D van Der Waals Metal Contacts and Their Circuits. *Adv. Mater.* *n/a* (n/a), 2109899. <https://doi.org/10.1002/adma.202109899>.
- (31) Wang, Y.; Kim, J. C.; Wu, R. J.; Martinez, J.; Song, X.; Yang, J.; Zhao, F.; Mkhoyan, A.; Jeong, H. Y.; Chhowalla, M. Van Der Waals Contacts between Three-Dimensional Metals and Two-Dimensional Semiconductors. *Nature* **2019**, *568* (7750), 70–74. <https://doi.org/10.1038/s41586-019-1052-3>.
- (32) Chen, S.-Y.; Goldstein, T.; Taniguchi, T.; Watanabe, K.; Yan, J. Coulomb-Bound Four- and Five-Particle Intervalley States in an Atomically-Thin Semiconductor. *Nat. Commun.* **2018**, *9* (1), 3717. <https://doi.org/10.1038/s41467-018-05558-x>.
- (33) Courtade, E.; Semina, M.; Manca, M.; Glazov, M. M.; Robert, C.; Cadiz, F.; Wang, G.; Taniguchi, T.; Watanabe, K.; Pierre, M.; Escoffier, W.; Ivchenko, E. L.; Renucci, P.; Marie, X.; Amand, T.; Urbaszek, B. Charged Excitons in Monolayer WSe₂: Experiment and Theory. *Phys. Rev. B* **2017**, *96* (8), 085302. <https://doi.org/10.1103/PhysRevB.96.085302>.
- (34) Edelberg, D.; Rhodes, D.; Kerelsky, A.; Kim, B.; Wang, J.; Zangiabadi, A.; Kim, C.; Abhinandan, A.; Ardelean, J.; Scully, M.; Scullion, D.; Embon, L.; Zu, R.; Santos, E. J. G.; Balicas, L.; Marianetti, C.; Barmak, K.; Zhu, X.; Hone, J.; Pasupathy, A. N. Approaching the Intrinsic Limit in Transition Metal Diselenides via Point Defect Control. *Nano Lett.* **2019**, *19* (7), 4371–4379. <https://doi.org/10.1021/acs.nanolett.9b00985>.
- (35) Chen, Y.-H.; Cheng, C.-Y.; Chen, S.-Y.; Rodriguez, J. S. D.; Liao, H.-T.; Watanabe, K.; Taniguchi, T.; Chen, C.-W.; Sankar, R.; Chou, F.-C.; Chiu, H.-C.; Wang, W.-H. Oxidized-Monolayer Tunneling Barrier for Strong Fermi-Level Depinning in Layered InSe Transistors. *Npj 2D Mater. Appl.* **2019**, *3* (1), 1–7. <https://doi.org/10.1038/s41699-019-0133-3>.
- (36) Irfan, I.; James Turinske, A.; Bao, Z.; Gao, Y. Work Function Recovery of Air Exposed Molybdenum Oxide Thin Films. *Appl. Phys. Lett.* **2012**, *101* (9), 093305. <https://doi.org/10.1063/1.4748978>.
- (37) Allain, A.; Kis, A. Electron and Hole Mobilities in Single-Layer WSe₂. *ACS Nano* **2014**, *8* (7), 7180–7185. <https://doi.org/10.1021/nn5021538>.
- (38) Cui, X.; Shih, E.-M.; Jauregui, L. A.; Chae, S. H.; Kim, Y. D.; Li, B.; Seo, D.; Pistunova, K.; Yin, J.; Park, J.-H.; Choi, H.-J.; Lee, Y. H.; Watanabe, K.; Taniguchi, T.; Kim, P.; Dean, C. R.; Hone, J. C. Low-Temperature Ohmic Contact to Monolayer MoS₂ by van Der Waals Bonded Co/h-BN Electrodes. *Nano Lett.* **2017**, *17* (8), 4781–4786. <https://doi.org/10.1021/acs.nanolett.7b01536>.

- (39) Allain, A.; Kang, J.; Banerjee, K.; Kis, A. Electrical Contacts to Two-Dimensional Semiconductors. *Nat. Mater.* **2015**, *14* (12), 1195–1205.
<https://doi.org/10.1038/nmat4452>.

TABLE OF CONTENTS/ABSTRACT GRAPHICS



FIGURES

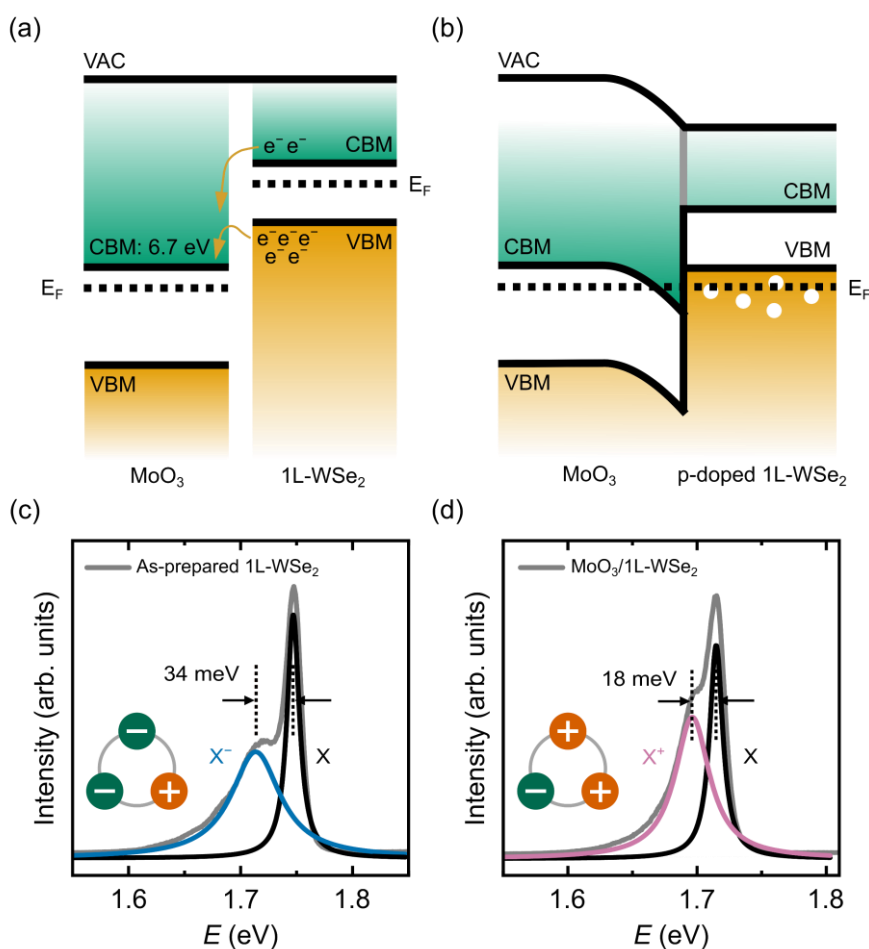


Figure 1. (a-b) Schematic band diagrams of isolated MoO_3 and 1L- WSe_2 (a), and MoO_3 and 1L- WSe_2 when they are in contact (b). 1L- WSe_2 is degenerate p-doped due to the surface charge transfer at the MoO_3 /1L- WSe_2 interface. (c-d) Low temperature photoluminescence (PL) spectra of as-prepared 1L- WSe_2 (c) and MoO_3 /1L- WSe_2 heterostructure (d). The spectra were taken at $T = 80$ K. X, X^- , and X^+ represent neutral excitons, negative trions, and positive trions,

respectively. The insets show the schematic of negative trions (electron plus exciton) and positive trions (hole plus exciton). The $\text{MoO}_3/1\text{L-WSe}_2$ heterostructure exhibits a strong PL signal from positive trions, suggesting a prevalent p-type doping due to the high electron affinity MoO_3 .

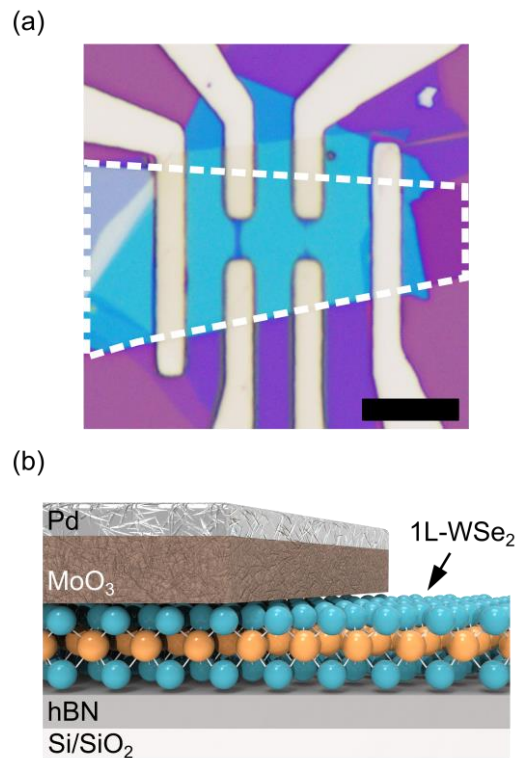


Figure 2. (a) Optical micrograph of a MoO_3 contacted 1L- WSe_2 FET with multiple electrodes. The 1L- WSe_2 nanoflake is indicated by the white dash line. The channel length and width are 19 and 14.4 μm , respectively. The distance between four-probe voltage V_{4p} probes is 7 μm . Scale bar: 10 μm . (b) A cross-sectional schematic of MoO_3 contacted 1L- WSe_2 FETs.

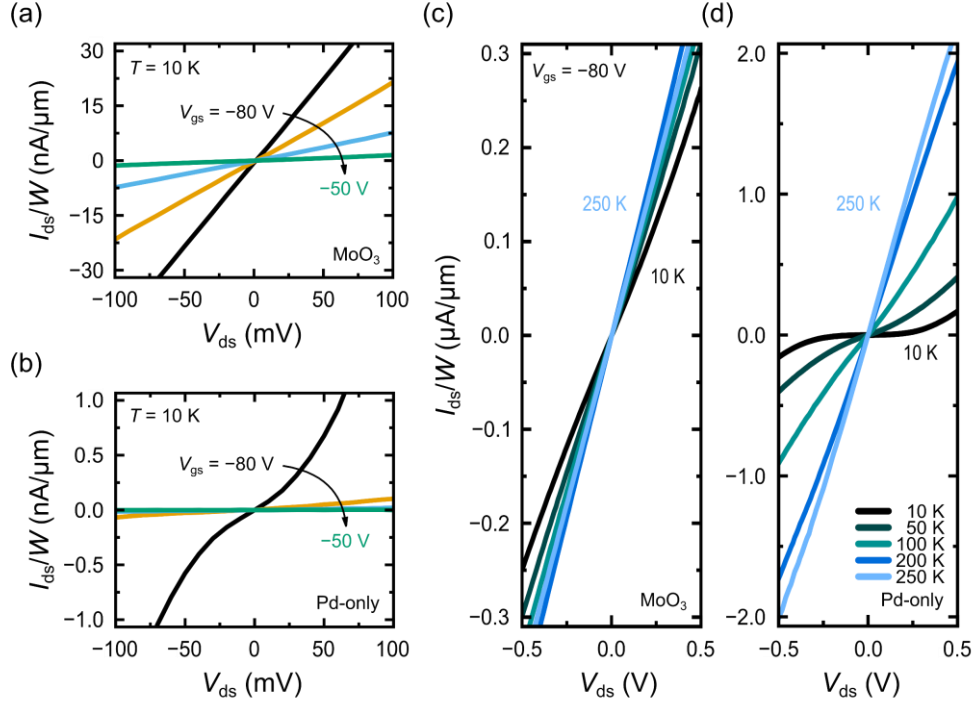


Figure 3. Transport characteristics of 1L-WSe₂ FETs with MoO₃ and Pd-only contacts. (a-b) Output curves at $T = 10$ K and gate voltage V_{gs} ranging from -80 V to -50 V with an increment of 10 V for 1L-WSe₂ FETs with MoO₃ contacts (a) and Pd-only contacts (b). (c-d) Temperature-dependent output curves at gate voltage $V_{gs} = -80$ V for 1L-WSe₂ FETs with MoO₃ contacts (c) and Pd-only contacts (d).

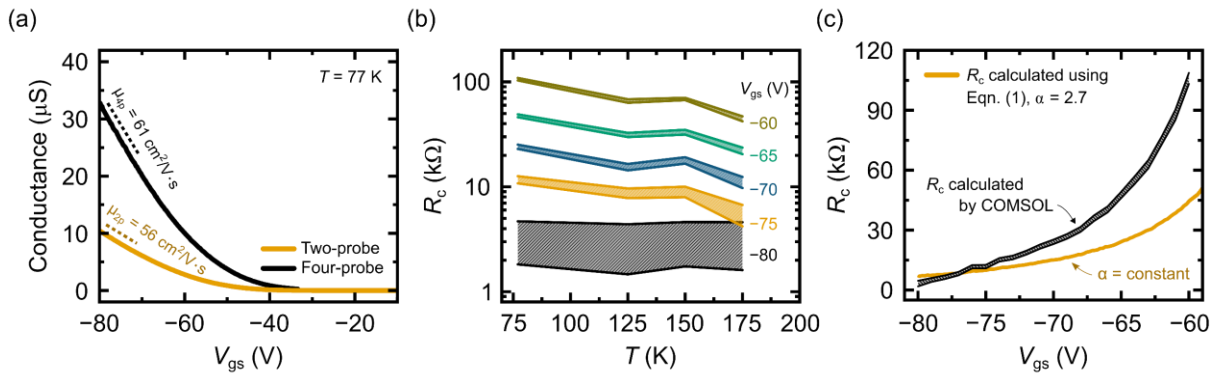


Figure 4. Transport characteristics of a MoO₃ contacted 1L-WSe₂ FET. (a) Drain current I_{ds} as a function of gate voltage V_{gs} at $T = 77$ K obtained by two- and four-terminal measurement. Drain voltage $V_{ds} = 1$ V (b) Calculated contact resistance R_c as a function of temperature at gate voltage V_{gs} ranging from -60 V to -80 V. (c) Contact resistance R_c as a function of gate voltage

V_{gs} at $T = 77$ K calculated by COMSOL (grey shaded area) and assuming a constant α , $\alpha = 2.7$ (orange solid line).

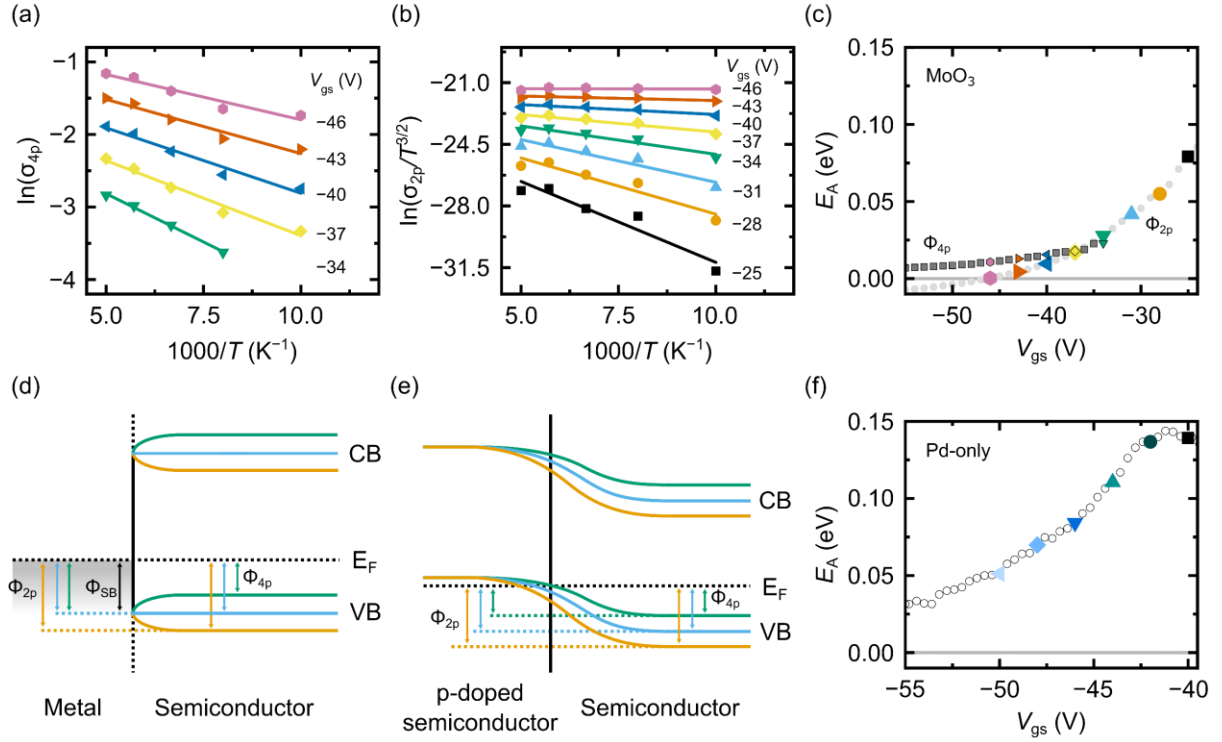


Figure 5. (a-b) Arrhenius plots of σ_{4p} (a), $\sigma_{2p}/T^{3/2}$ (b) for a 1L-WSe₂ FET with MoO₃ contacts. σ_{2p} is two-probe conductivity, σ_{4p} is four-probe conductivity, and T is the temperature. (c) Inferred activation energies E_A of bulk channel and contact, Φ_{4p} and Φ_{2p} respectively, as functions of gate voltage V_{gs} for the MoO₃ contacted 1L-WSe₂ FET extracted from (a, b). (d, e) band diagram for metal/semiconductor interface (d) and the interface between p-doped semiconductor and semiconductor (e), showing schematically the variation of Φ_{4p} and Φ_{2p} with gate voltage (different coloured lines; orange more positive V_{gs} , blue intermediate V_{gs} , green more negative V_{gs}). (f) Inferred activation energies E_A as functions of gate voltage V_{gs} for a 1L-WSe₂ with Pd-only contacts.